RSC Advances




ROYAL SOCIETY OF CHEMISTRY

www.rsc.org/advances

# Activated carbon with micrometer-scale channels prepared from luffa sponge fibers and their application for supercapacitors

Jianpeng Li, Zhonghua Ren, Yaqi Ren, Lei Zhao, Shuguang Wang and Jie Yu*

Table of Content image and illustration

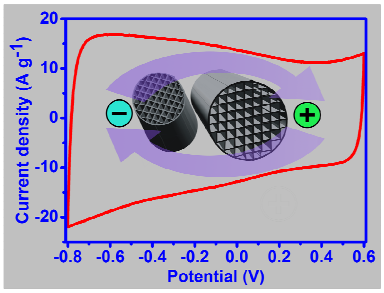


Activated carbon with dense and parallel arranged macrochannels is prepared from luffa sponge fibers for supercapacitor application.

# Activated carbon with micrometer-scale channels prepared from luffa sponge fibers and their application for supercapacitors

**Jianpeng Li, Zhonghua Ren, Yaqi Ren, Lei Zhao, Shuguang Wang, *and* Jie Yu***

Shenzhen Engineering Lab of Flexible Transparent Conductive Films, Shenzhen Key Laboratory for Advanced Materials, Department of Material Science and Engineering, Shenzhen Graduate School, Harbin Institute of Technology, University Town, Shenzhen 518055, China.
*Corresponding author. E-mail: jyu@hitsz.edu.cn

In this paper, we report preparation of macrochanneled activated carbon (MCAC) with novel structure combining micropores, mesopores, and macrochannels and its electrochemical property for supercapacitor application. The MCAC was prepared by carbonizing luffa sponge fibers and subsequent activation with KOH. The MCAC has densely packed and parallel channels of 4-10 μm in diameter and 0.3-1 μm in wall thickness, which was inherited from the natural structure of the luffa sponge fibers. Micro- and mesopores were produced on the inner surface of the channel walls, forming a hierarchically porous structure. The MCAC exhibits excellent electrochemical performance for application as electrode materials of supercapacitors in appropriate electrolytes. The specific capacitances of the MCAC at 1 A $g^{-1}$ are 167, 196, and 249 F $g^{-1}$ in $Na_2SO_4$, KOH, and $H_2SO_4$ solutions, respectively. The MCAC materials reported here may have broad applications such as supercapacitors, catalysis, and templates for supporting various functional materials.

## Introduction

Supercapacitors are highly promising in many important applications such as portable electronics and electric vehicles due to the advantages of high power capability, long cycle life, fast charge/discharge rate, low cost, and environmental friendliness.[1-4] Activated carbon (AC) has been used for commercial production of supercapacitors due to its low cost and high porosity. The capacitance of the AC comes from the charge accumulation at the electrode/electrolyte interface, and therefore depends on the porous structure of the electrode such as pore size and accessible surface area.[5-8] Micropores (<2 nm) can generate high specific surface area (SSA) and provide more active sites for electrolyte ion adsorption.[9] Mesopores (2–50 nm) are necessary for efficient transport of electrolyte into the micropore.[10] Although macropores do not contribute greatly to the SSA of AC, they are important for electrolyte transportation deep into the carbon particles,[11] and thus increasing the utilization ratio of the active materials. The AC is mainly microporous and devoid of the electrolyte transport path towards the interior of the carbon particles. Consequently, only the surface layer of the AC particles and the electrode structure contribute to the capacitance, leaving the interior as dead materials.[12] Recently, many efforts have been devoted to the rational design and preparation of macroporous carbon materials using templates, showing

good effects in improving the electrochemical performance.[13-16] But the template route suffers from the problems of process complexity and low output, further work is necessary to find new route to prepare the porous carbon with appropriate pore structure.

Biological materials possess a rich variety of microstructures,[17-19] which provide precursors for preparing carbon materials with different structures. Recently, plant materials with the advantages of low cost and environmental friendliness have been used to prepare new carbon materials with unique structure and property for supercapacitor application.[20-23] Among the different plant materials, luffa sponge fibers have unique structure, containing many micrometer-scale channels with dense and parallel arrangement.[24] It is expected that the luffa sponge fibers are very attractive as the precursor to prepare hierarchically porous carbon materials combining subnano- to micrometer-scale features. However, to the best of our knowledge, preparation of carbon materials from luffa sponge fibers for supercapacitor application has not been reported yet.

In this paper, macrochanneled activated carbon (MCAC) was prepared from the luffa sponge fibers for application as electrode materials of supercapacitors. The macrochannels in the MCAC are densely arranged and parallel each other with diameters at micrometer-scale. Micro- and mesopores were generated on the inner surface of the channel walls, forming a hierarchically porous structure. The MCAC exhibits excellent electrochemical performance for application as electrode materials for supercapacitors in aqueous electrolyte. This is the first time to report the carbon materials derived from the luffa sponge fibers for supercapacitor application. Considering the abundance of the luffa sponge, the present MCAC materials are highly promising in various applications such as supercapacitors, electrocatalysts, and templates for growing various functional materials.

## Experimental

### Materials preparation

The luffa sponge was collected from South China Plant Home in Guangzhou. Before carbonization the luffa sponge was washed with water and dried at 60 ºC. The carbonization of the luffa sponge was conducted in a conventional tube furnace. In a typical process, 10 g of luffa sponge fibers were heated for 2 h at different temperatures (700, 800, and 900 ºC) in $NH_3$ atmosphere with a flow rate of 60 mL $min^{-1}$. Subsequently, the carbonized samples were activated for 90 min with KOH in $N_2$ at 750 $^oC$ with a heating rate of 8 $^oC$ $min^{-1}$. The mass ratio of carbon to KOH during the activation is 1:2. Afterwards, the activated samples were washed in sequence with 1 M HCl and distilled water to remove the residue KOH and dried at 60 $^oC$, obtaining the MCAC samples. The above MCAC samples are denominated as $AC700NH_3$, $AC800NH_3$ and $AC900NH_3$, respectively, depending on the carbonization temperature. The sample carbonized at 800 ºC in $NH_3$ without activation is called $C800NH_3$. For comparison, the sample was also prepared by carbonization in $N_2$ at 800 ºC and activated in $N_2$ at 750 ºC, which we call $AC800N_2$.

### Structure characterization

Scanning electron microscope (SEM, HITACHI S-4700), transmission electron microscope (TEM, JEM-2100HR), Raman spectroscopy (Renishaw RM-1000), and X-ray diffraction (XRD, Rigaku D/Max 2500/PC) were used to characterize the morphology and structure of the samples. X-ray photoelectron spectroscopy (XPS, ESCALAB 250) and Fourier transform infrared spectroscopy (FTIR, Thermo NIR-Antaris II FTIR spectrometer) were used to determine the composition and bonding states of the samples. Nitrogen sorption isotherms were measured at 77 K with a Micromeritics Tristar 3000 analyzer (USA). Before measurements, the samples were degassed in vacuum at 200 ºC for 6 h. The SSA were calculated by the Brunauer–Emmett–Teller (BET) method. The pore sizes ($D_p$) were calculated from the adsorption branches of the isotherms using the Barrett–Joyner–Halenda (BJH) model.

**Electrochemical measurement**

The electrochemical data were collected on a three-electrode electrochemical cell. A platinum wire (CHI115) and an Ag/AgCl (sat.) (CHI111) electrode act as the counter and reference electrode, respectively. For preparing the working electrodes, 8 mg MCAC powders and 1 mg acetylene black were mixed in 1 ml ethanol to form slurry. Then an appropriate amount of the slurry was spread on the surface of a glassy carbon electrode and dried in air. Afterwards, a drop of nafion solution (5 wt.%) was dripped onto the dried slurry, obtaining the working electrode. Three different electrolytes (1 M $Na_2SO_4$, 6 M KOH, and 1 M $H_2SO_4$) were used for the electrochemical tests. Cyclic voltammogram (CV) curves, galvanostatic charge/discharge (CD) curves, and electrochemical impedance spectra (EIS) were measured by a CHI 660D electrochemical work station (Shanghai CH Instruments Co., China). The operation stabilities were measured by a battery measuring system (CT2001A, Wuhan Land Electronics Co. Ltd.).

The energy density and power density of the supercapacitors were calculated by the following equations:

$$C = \frac{I \times \Delta t}{M_s \times \Delta V}$$

$$E = \frac{1}{2} \times C \times (\Delta V)^2$$

$$P = \frac{E}{\Delta t}$$

where $C$ (F $g^{-1}$) is the specific capacitance of the active material, $I$ is discharging current (A), $\Delta V$ is the potential window of discharge (V), $\Delta t$ is discharging time ($s$), $M_s$ is the mass of the active materials (g). $E$ (Wh/kg ) refers to the energy density (converting to Wh/kg after divided by 3.6), $P$ (W/kg) is power density.

## Results and discussion

Luffa sponge consists of many interlaced continuous fibers, exhibiting a three-dimensional network structure (Fig. 1a). After carbonization, these fibers broke and the network structure collapsed. The yield after carbonization in $NH_3$ at 800 ºC is about 16.8%, which further decreases to 9.3% after activation. It was found that the morphology of the MCAC samples prepared under different carbonizing atmospheres

and temperatures is about similar. Fig. 1b-e shows the SEM images of the AC800$NH_3$ sample, which is representative of the samples obtained at different temperatures and atmospheres. It is observed that the MCAC products are short broken fibers with diameters in the range of 150-450 μm (Fig. 1b). On the cross section of the broken fibers many densely packed parallel channels can be observed, exhibiting a honeycomb-like porous structure (Fig. 1c and d). These channels are polygonal in shape with the diameter ranging from 4 to 10 μm and wall thickness about 0.3-1 μm (Fig. 1e and f). Comparing with the channel diameter, the channel walls are very thin, generating very large hollow space. These morphology features are derived from the luffa fiber precursor.[25] The macrochannels with straight and smooth walls provide convenient pathways for electrolyte solution transfer. Fig. 2 shows the TEM images of the AC800$NH_3$ sample. These images were taken from the edge area with small thickness of a channel wall. It is observed that the sample surface is very rough with nanoscale cavities, which should be generated during activation (Fig. 2a). The high resolution TEM image shows that the MCAC is highly defective with desultory and distorted lattice fringes (Fig. 2b). This structure is typical of the carbon materials thermally converted from the plant material precursor.[20, 26-27]

XRD and Raman spectra were measured to further investigate the structure of the MCAC materials derived from the luffa sponge fibers. Fig. 3a shows the XRD patterns of the samples prepared under different conditions. For all of these patterns two broad peaks can be observed, which are characteristic of turbostratic carbon structure. For the AC samples carbonized in $NH_3$ (Fig. 2a-III, IV and V) the two peaks locate around 23.0-25.0$^o$ and 43.0-43.5$^o$, corresponding to the diffraction of (002) and (10) planes of the turbostratic carbon structure, respectively. It is observed that the diffraction peaks are very weak at 700 $^o$C, suggesting very low crystallization degree at this temperature. At 800 and 900 $^o$C the peak intensities increase greatly and with increasing the carbonizing temperature the peak narrows slightly with the position shifting towards higher angle, showing the corresponding improvement of the crystallinity. Comparing with the AC800$NH_3$, the peak width of the AC800$N_2$ decreases obviously, indicating better crystallinity for the carbonization in $NH_3$ than in $N_2$. This may be because $NH_3$ can disassociate into active species such as atomic H, NH, and $NH_2$, which promoted the crystallizing process by bonding with the carbon atoms to increase their mobility.[28] Fig. 3b shows the Raman spectra of the different samples. The two strong peaks located at around 1349 and 1596 $cm^{-1}$ are the D and G peaks characteristic of carbon materials,[29] respectively. The intensity ratio of D to G peak ($I_D/I_G$) denotes the degree of structural order relative to a perfect graphitic structure. The $I_D/I_G$ ratios were calculated by Lorentzian fitting to be 1.89, 2.01, 2.63, 1.52, and 1.23 for C800$NH_3$, AC800$N_2$, AC700$NH_3$, AC800$NH_3$, and AC900$NH_3$, respectively. For the AC samples carbonized in $NH_3$ (Fig. 3b-III, IV, VI) the $I_D/I_G$ ratio decreases markedly with increasing the carbonizing temperature, indicating better crystallinity at higher temperature. Meanwhile, the full width at half maximum (FWHM) of the G peak decreases with increasing the carbonizing temperature, similarly related to the crystallinity improvement at higher temperature.[30] The lower $I_D/I_G$ ratio for AC800$NH_3$ than AC800$N_2$ confirms the promoting effect of $NH_3$ on

crystallinity.[28] The present Raman results is in accordance with those indicated by the XRD patterns.

Fig. 3c shows the $N_2$ adsorption/desorption isotherms of the different samples. The calculated structure parameters of the pores are listed in Table 1. All the samples exhibit type-I absorption isotherms with saturation at low relative pressure and plateau over a wide range of relative pressure, which is typical of the micropores. The C800$NH_3$ also exhibits some adsorption capacity despite no activation process. This should be caused by the rough surface generated by the etching reaction of $NH_3$ during carbonization.[28, 31] After activation, the $N_2$ adsorption capacity of the samples increases dramatically. For the three MCAC samples carbonized in $NH_3$ (Fig. 3c-III, IV, V) the AC800$NH_3$ exhibits the highest adsorption capacity. It can be seen that the pore structure obtained during the activation is dependent on the structure of the carbon materials generated during the carbonization. At too low carbonizing temperature (700 $^oC$) too much defect exists in the carbon structure, which may be too weak to support the shape of the micropores, leading to the lower SSA. As shown in Table 1, the SSA of AC800$NH_3$ reaches 1510.7 $m^2 g^{-1}$ with a total pore volume of 0.74 $cm^3 g^{-1}$, which is mainly contributed by micropores. At higher carbonizing temperature (900 $^oC$) the obtained carbon materials have higher crystallinity, which provides higher resistance towards the chemical attack and reduces the pore production. In contrast to AC800$NH_3$, the AC800$N_2$ exhibits a SSA of 1371.5 $m^2 g^{-1}$ and total pore volume of 0.53 $cm^3 g^{-1}$, suggesting that $NH_3$ is an effective erosive gas for developing rough surface. The pore size distribution estimated from the adsorption branches using the BJH model is shown in Fig. 3d. It is clearly indicated that the pore distribution is mainly below 2 nm with a considerable proportion of mesopores. The hierarchical porous structure combining the abundant micropores, mesopores, and macrochannels may result in well match between ion adsorption and transport.

XPS and FTIR spectra were measured to determine the composition and bonding states of the samples. Fig. 4a-c shows the XPS and N1s spectra of the AC800$N_2$ and AC800$NH_3$. It is indicated that both samples contain C, O, and N elements. The O component should mainly originate from the O element contained in the luffa sponge precursor, ambient atmosphere during carbonization and activation, and the activating agent KOH. The N component is from that contained in the luffa sponge precursor and $N_2$ and $NH_3$ introduced during carbonization and activation. It has been known that N can be doped into the graphitic structure in the forms of pyridinic-N, pyrrolic-N, graphitic-N, and pyridine-N-oxide with the XPS peaks at 398.1-399.3, 399.8-401.2, 401.1-402.7, and 402–405 eV,[32] respectively. The doping forms of N and their relative proportions were analyzed by deconvoluting the N1s peaks and shown in Fig. 4b and c and Table 2. It is found that all the four forms of the doped N are present in the two samples. But the sample carbonized in $NH_3$ has higher N concentration, which results from the higher reactivity of $NH_3$ than $N_2$. The application of $NH_3$ during carbonization is for doping the MCAC with N because of its high reaction activity. The activation process was also carried out in $NH_3$ for both the carbon materials carbonized in $NH_3$ and $N_2$. It was found that the SSA and capacitance of the MCAC activated in $NH_3$ is lower. This is because the pore structure was partially destroyed

by $NH_3$ during the activation process due to its high etching reactivity. Therefore, for balancing the two factors of obtaining high SSA and N doping the carbonization was performed in $NH_3$ and the activation was performed in $N_2$. FTIR spectra also indicate the presence of the functional groups related to C, O, and N including C-O-H,[33] C=N,[34] and O-H (Fig. 4d). The presence of the doped N and O will improve the supercapacitive performance of the MCAC materials by bringing pseudoreactions and improving the wettability.

The electrochemical performance of the MCAC samples were evaluated by CV curves, galvanostatic CD curves, and EIS spectra in the aqueous solutions of 1 M $Na_2SO_4$, 6 M KOH, and 1 M $H_2SO_4$. As shown in Fig. 5a, the CV curves of all the MCAC samples present quasi-rectangular shape at a scan rate of 20 mV $s^{-1}$ in 1 M $Na_2SO_4$, implying the typical capacitive behavior. The current response of the CV curves increases in the order of C800$NH_3$, AC700$NH_3$, AC800$N_2$, AC900$NH_3$, and AC800$NH_3$. The AC800$NH_3$ exhibits the largest current response, corresponding to the largest capacitance. It is clearly indicated that the CV current density is greatly dependent on the SSA of the samples. As the AC800$NH_3$ possesses the highest SSA, we measured the CV curves of this sample at different scan rate in different electrolyte, which is shown in Fig. 5b-d. It can be seen that the rectangular shape is maintained in different electrolytes except slight distortion at high scan rates in KOH solution, indicating good rate capability and capacitive behavior. It is noted that all the samples exhibit a high working voltage of 1.4 V in $Na_2SO_4$ solution, which was determined by carefully comparing the CV curves of the samples at different voltage window. This high voltage is mainly ascribed to the neutral character of the applied electrolyte. Up to now, high working voltage from 1.6 V to 2.2 V has been reported for supercapacitors in neutral electrolyte.[28, 35-38] It has been proposed that the low and equal $H^+/OH^-$ concentrations and the high salvation energy of both the alkali metal cations and sulfate anions competitive with the water decomposition energy inhibit the gas evolution reaction in the neutral electrolyte, and thus enlarge the working voltage.[36-38] The high working voltage is important for achieving high energy density and reducing the series number of the devices in application.

Electrochemical impedance spectroscopy is a powerful tool to establish the relationship between the electrochemical performance of the electrode materials and their structure. The EIS spectra were measured for the samples in the frequency range of 0.01-100 kHz with an AC perturbation of 5 mV. Fig. 6a shows the EIS spectra of the different MCAC samples in $Na_2SO_4$ solution. It can be seen that all the Nyquist plots exhibit about similar shape comprising an arc in the high frequency region, a Warburg section with a slope of 45$^o$ in the middle frequency, and a straight line in low frequency region. The arc results from the parallel connection of double-layer capacitance and charge transfer resistance ($R_{Ct}$) at the electrode/electrolyte interface.[39] The high frequency intersection of the arc with the real axis corresponds to the internal resistance including the ionic resistance of the electrolyte, electrical resistance of the electrode, and interfacial resistance between the electrode and electrolyte.[40-41] The internal resistance determines charge/discharge rate of the supercapacitors. The Warburg section results from the frequency dependence of ion diffusion in the

electrolyte to the electrode structure.[42] The straight line in low frequency represents the ion diffusion resistance in the active materials.[43-44] All the samples show the characteristics of the capacitive charge storage mechanism. Among the different samples, the AC800$NH_3$ has the smallest high frequency intercept with the real axis, smallest arc size, shortest Warburg section, and vertical straight line in the low frequency, suggesting the best charge storage behavior with the electrical double layer capacitive mechanism. This should be resulted from the combination of the high SSA, better conductivity, and presence of the macrochannels. Fig. 6b shows the EIS spectra of the AC800$NH_3$ in the different electrolyte solutions, which present different electrochemical behavior depending on the electrolyte type. It is observed that for the different electrolytes the internal resistance increases in the order of KOH, $H_2SO_4$, and $Na_2SO_4$. This is caused by the difference of the ionic conductivity for the three different electrolytes. We have measured the ionic conductivity of the different electrolyte solutions, which are 626 mS $cm^{-1}$, 460 mS $cm^{-1}$, and 89 mS $cm^{-1}$ for 6 M KOH, 1 M $H_2SO_4$, and 1 M $Na_2SO_4$ solutions, respectively. The internal resistance measured in the three different electrolytes is well consistent with the difference of their ionic conductivity. Because the discrepancy of the ionic conductivity is relatively small for the KOH and $H_2SO_4$ electrolytes the internal resistances in the two electrolytes are approaching. It is noted that the low frequency straight line in $Na_2SO_4$ solution is almost vertical to the real axis while those in KOH and $H_2SO_4$ solutions are much more inclined. We believe that this is caused by the difference of the ion diameter for the three different electrolytes. It is known that the diameters of the solvated $K^+$ and $H_3O^+$ are close[45-46] but smaller than the solvated $Na^+$.[47] Therefore, the solvated $K^+$ and $H_3O^+$ ions can penetrate larger depth into the pores than the solvated $Na^+$ ions. When the frequency of the applied potential decreases to a certain low value the accessible pore surface will be completely utilized for the larger $Na^+$ and the ion adsorption does not change with further decreasing the frequency, forming a vertical line in the low frequency of the Nyquist plot. However, for the similar low frequency range the penetrating depth of the smaller $K^+$ and $H_3O^+$ ions can still increase with further decreasing the frequency, exhibiting a sloping line depending on the frequency of the applied potential.

Fig. 7a displays the galvanostatic CD curves of the different samples at the current density of 1 A $g^{-1}$ in $Na_2SO_4$ solution. All the curves exhibit nearly isosceles triangle shape. The specific capacitances were calculated from the discharging curves, being 67, 141,135, 167, and 150 F $g^{-1}$ for C800$NH_3$, AC800$N_2$, AC700$NH_3$, AC800$NH_3$, and AC900$NH_3$, respectively. The CD curves were measured in the three different electrolytes for AC800$NH_3$ at different current densities, which are shown in Fig. 7b-d. The calculated specific capacitances are 162, 155, and 143 F $g^{-1}$ at the current densities of 2, 5, and 10 A $g^{-1}$ in $Na_2SO_4$ solution, 196, 185, and 156 F $g^{-1}$ at the current densities of 1, 2, and 5 A $g^{-1}$ in KOH solution, and 249, 215, and 197 F $g^{-1}$ at the current density of 1, 2, and 5 A $g^{-1}$ in $H_2SO_4$ solution, respectively. It is found that the MCAC simply derived from the luffa sponge fibers possess high specific capacitance in different electrolytes, especially in $H_2SO_4$.

Operation stability of supercapacitors is a crucial parameter for their practical

application. To investigate the electrochemical stability of $AC800NH_3$, long-term charge/discharge measurements were performed at a current density of 1A $g^{-1}$ in 1 M $Na_2SO_4$, 6 M KOH, and 1 M $H_2SO_4$ solutions, respectively, Fig. 8 shows the cycling behavior of $AC800NH_3$ in different electrolytes for 5000 times. It is indicated that the $AC800NH_3$ has good cycling stability in $Na_2SO_4$ and KOH solutions with the capacitance retention of 95.7% and 95.0% after 5000 cycles. The capacitance retention after 5000 cycles in $H_2SO_4$ solution is 87.6%. Taking into account the high working voltage of 1.4 V in $Na_2SO_4$ solution and the erosive nature of the KOH and $H_2SO_4$ solutions, the above stability values are high, which we ascribed to the superior structure of the MCAC. Because the active sites are located on the inner surface of the channels the capacitance loss caused by the mechanical damage of the active surface during operation could be avoided. For example, even if some parts of the surface layer peel during operation they can still keep contact with the channel walls and work as active materials.

The present work indicates that the MCAC prepared from the common luffa sponge possesses excellent electrochemical performance, much better that the conventional activated carbon. It is considered that the presence of the macrochannels accounts for the improvement of the electrochemical performance. The MCAC integrates the micropores, mesopores, and macrochennels. The micropores act as the active sites for ion adsorption and charge storage, the mesopores provide pathways for ion transport, whereas the macrochannels allow the electrolyte solution to flow freely deep into the carbon particles, and therefore increase the utilization ratio of the active materials. Additionally, the doped N and O also contribute to the capacitance by introducing pseudoreactions and improving the wettability.

In order to evaluate the practicability of the obtained materials we assembled symmetric supercapacitors using the $AC800NH_3$ as the electrode materials and 1 M $Na_2SO_4$ aqueous solution as the electrolyte. Fig. 9a shows the CV curves of the supercapacitor at scan rates ranging from 5 to 100 mV $s^{-1}$. These CV curves exhibit nearly rectangular shape at all the scan rates, suggesting the capacitive mechanism of charge storage. The galvanostatic CD curves at different current density show nearly triangular shape (Fig. 9b), which also indicates that the capacitive mechanism dominates the charge storage. The energy density of the fabricated supercapacitors was calculated to be 10.3 Wh $kg^{-1}$ from the galvanostatic CD curve at the power density of 700 W $kg^{-1}$. To demonstrate the application potential of the MCAC materials two supercapacitors in series were used to power a LED. Each supercapacitor contains 2 mg of the active materials ($AC800NH_3$). After charging the tandem devices at 5 A $g^{-1}$, the LED can light for 7 seconds. It can be seen that the MCAC materials are of high promise for practical application.

## Conclusion

In conclusion, the MCAC materials with unique structure integrating macrochannels, micropores, and mesopores have been prepared from luffa sponge fibers by carbonization and activation for supercapacitor application. The macrochannels are inherited from the natural structure of the luffa sponge fibers, which are parallel each

other with the diameter ranging from 4 to 10 μm and wall thickness about 0.3-1 μm. The MCAC exhibits excellent electrochemical performance including high specific capacitance and high operation stability in appropriate electrolytes, which is much better than the conventional activated carbon. The combination of the macrochannels, micropores, and mesopores accounts for the improvement of the electrochemical performance. The presence of the macrochannels allow the electrolyte solution to flow freely deep into the carbon particles, and thus increasing the utilization ratio of the active materials. Activation to generate enough active sites is necessary for improving the electrochemical performance. We here demonstrate that the luffa sponge is a good precursor for preparing the carbon materials with unique structure and attractive for various applications such as supercapacitors, electrocatalysts, and templates for supporting various functional materials.

**Acknowledgements**

This work is supported by the National Basic Research Program of China (2012CB933003), National Natural Science Foundation of China (No. 51272057), and Shenzhen Basic Research Program (JCYJ20130329150737027).

**Notes and references**

1 E. Frackowiak, *Phys. Chem. Chem. Phys.*, 2007, **9**, 1774-1785.
2 P. Simon and Y. Gogotsi, *Nat. Mater.*, 2008, **7**, 845-854.
3 X. F. Wang, B. Liu, Q. F. Wang, W. F. Song, X. J. Hou, D. Chen, Y. B. Chen and G. Z. Shen, Adv. Mater., 2013, 25, 1479-1486.
4 G. P. Wang, L. Zhang and J. J. Zhang, *Chem. Soc. Rev.*, 2012, **41**, 797-828.
5 W. S. Chae, D. V. Gough, S. K. Ham, D. B. Robinson and P. V. Braun, *ACS Appl. Mater. Inter.*, 2012, **4**, 3973-3979.
6 J. S. Huang, B. G. Sumpter and V. Meunier, *Chem. Eur. J.*, 2008, **14**, 6614-6626
7 J. S. Huang, B. G. Sumpter and V. Meunier, *Angew. Chem. Int. Ed.*, 2008, **47**, 520-524.
8 S. Chen, W. Xing, J. J. Duan, X. J. Hu and S. Z. Qiao, *J. Mater. Chem. A.*, 2013, **1**, 2941-2954.
9 E. Frackowiak and F. Beguin, *Carbon*, 2001, **39**, 937-950.
10 J. Chmiola, C. Largeot, P. L. Taberna, P. Simon and Y. Gogotsi, *Science*, 2010, **328**, 480-483.
11 D. W. Wang, F. Li, M. Liu, G. Q. Lu, and H. M. Cheng, *Angew. Chem. Int. Ed.*, 2008, **47**, 373-382.
12 I. H. Kim, J. H. Kim, K. B Kim, *Electrochem. Solid ST.*, 2005, **8**, A369-A372.
13 B. G. Choi, M. H. Yang, W. H. Hong, J. W. Choi and Y. S. Huh, *ACS Nano*, 2012, **6**, 4020-4028.
14 L. L. Zhang, S. Li, J. T. Zhang, P. Z. Guo, J. T. Zheng and X. S. Zhao, *Chem. Mater.*, 2010, **22**, 1195-1202.
15 P. Adelhelm, Y. S. Hu , L. Chuenchom, M. Antonietti, B. M. Smarsly and J. Maier, *Adv. Mater.*, 2007, **19**, 4012-4017.
16 S. H. Lee, H. W. Kim, J. O. Hwang, W. J. Lee, J. Kwon, C. W. Bielawski, R. S.

Ruoff and S. O. Kim, *Angew. Chem. Int. Ed.*, 2010, **122**, 10282-10286.
17 N. Huebsch and D. J. Mooney, *Nature*, 2009, **462**, 426-432
18 H. B. Yao, H. Y. Fang, X. H. Wang and S. H. Yu, *Chem. Soc. Rev.*, 2011, **40**, 3764-3785.
19 S. Sotiropoulou,Y. S. Sastre, S. S. Mark and C. A. Batt, *Chem. Mater*., 2008, **20**, 821-834.
20 E. Raymundo-Piñero, M. Cadek and F. Béguin, *Adv. Funct. Mater*., 2009, **19**, 1032-1039.
21 T. E. Rufford, D. Hulicova-Jurcakova, K. Khosla, Z. Zhu and G. Q. Lu, *J. Power Sources*, 2010, **195**, 912-918
22 M. Biswal, A. Banerjee, M. Deo and S. Ogale, *Energy Environ. Sci.*, 2013, **6**, 1249-1259.
23 L. Jiang, J. Yan, L. Hao, R. Xue, G. Sun and B. Yi, *Carbon*, 2013, **56**, 146-154.
24 K. E. Bal, Y. Bal, G. Cote and A. Chagnes, *Mater. Lett.*, 2012, **79,** 238-241.
25 A. Zampier, G. T. P. Mabande, T. Selvam, W. Schwieger, A. Rudolph, R. Hermann, H. Sieber and P. Greil, *Mater. Sci. Eng. C*, 2006, **26,** 130-135.
26 T. H. Wang, S. X. Tan and C. H. Liang, *Carbon*, 2009, **47,** 1867-1885.
27 J. Yang and K. Q. Qiu, *Chem. Eng. J.*, 2010, **165**, 209-217.
28 L. Zhao, Y. J. Qiu, J. Yu, X. Y. Deng, C. L. Dai and X. D. Bai, *Nanoscale*, 2013, **5**, 4902-4909.
29 M. A. Pimenta, G. Dresselhaus, M. S. Dresselhaus, L. G. Cançado, A. Jorioa and R. Saitoe, *Phy. Chem. Chem. Phy*., 2007, **9**, 1276-1290.
30 M. Chhowalla, A. C. Ferrari, J. Robertson and G. A. J. Amaratunga, *Appl. Phys. Lett*., 2000, **76**, 1419-1421.
31 Y. J. Qiu, J. Yu, T. N. Shi, X. S. Zhou, X. D. Bai and J. Y. Huang, *J. Power Sources*, 2011, **196**, 9862-9867.
32 H. B. Wang, T. Maiyalagan, X. Wang, *ACS Catal*., 2012, **2**, 781-794.
33 I. A. W. Tan, A. L. Ahmad, and B. H. Hameed, *J. Hazard. Mater.,* 2008, **153**, 709–717.
34 C. L. Mangun, K. R. Benak, J. Economy, and K. L. Foster, Carbon, 2001, 39, 1809-1820.
35 J. Xu, H. Wu, C. Xu, H. T. Huang, L. F. Lu, G. Q. Ding, H. L. Wang, D. F. Liu, G. Z. Shen, D. D. Li and X. Y. Chen, *Chem. Eur. J.*, 2013, **19**, 6451-6458.
36 K. Fic , G. Lota , M. Meller and E. Frackowiak, *Energy Environ. Sci.*, 2012, **5**, 5842-5850.
37 Y. K. Hsu, Y. C. Chen, Y. G. Lin, L. C. Chen and K. H. Chen, *J. Mater. Chem.*, 2012, **22**, 3383-3387;
38 L. Zhao, J. Yu, W. J. Li, S. G. Wang, C. L. Dai, J. W. Wu, X. D. Bai and C. Y. Zhi *Nano energy*, 2014, **4**, 39-48.
39 Z. P. Li, Y. J. Mi, X. H. Liu, S. Liu, S. R. Yang and J. Q. Wang, *J. Mater. Chem.*, 2011, **21**, 14706-14711.
40 B. Xu, S. F. Yue, Z. Y. Sui, X. T. Zhang, S. S. Hou, G. P. Cao and Y. S. Yang, *Energy Environ. Sci.*, 2011, **4**, 2826-2830.
41 Z. J. Fan, J. Yan, T. Wei, L. J. Zhi, G. Q. Ning, T. Y. Li and F. Wei, *Adv. Funct.*

*Mater.*, 2011, **21**, 2366-2375.
42 B. E. Conway and W. G.. Pell, *J. Power Sources*, 2002, 105, 169-181.
43 B. G. Choi, J. Hong, W. H. Hong, P. T. Hammond and H. Park, *ACS Nano*, 2011, **5**, 7205-7213.
44 Y. C. Qiu, X. F. Zhang and S. H. Yang, *Phys. Chem. Chem. Phys.*, 2011, **13**, 12554-12558.
45 D. Hulicova, M. Kodama, and H. Hatori, *Chem. Mater.*, 2006, **18**, 2318-2326.
46 L. Eliad, G. Salitra, A. Soffer and D. Aurbach, *J. Phys. Chem. B*, 2001, 105, 6880-6887.
47 M. Endo, T. Maeda, T. Takeda, Y. J. Kim, K. Koshiba, H. Hara and M. S. Dresselhaus, *J. Electrochem. Soc.*, 2001, **148**, A910-A914.

**Table Captions:**

Table 1. Table 1 Calculated total SSA ($S_{BET}$), SSA of micropores ($S_{micro}$), ratio of $S_{micro}$ to $S_{BET}$ ($R_m$), total pore volume ($V_{total}$), micropore volume ($V_{micro}$), and average pore diameter ($D_p$).

Table 2 Concentrations (*at.* %) of C, O, and N in the different samples and binding energy (B.E., eV) and relative proportions (R.P., %) of the different forms of the doped N obtained by fitting the XPS peaks.

**Table 1** Calculated total SSA ($S_{BET}$), SSA of micropores ($S_{micro}$), ratio of $S_{micro}$ to $S_{BET}$ ($R_m$), total pore volume ($V_{total}$), micropore volume ($V_{micro}$), and average pore diameter ($D_p$).

| sample | $S_{BET}$ ($m^2\ g^{-1}$) | $S_{micro}$ ($m^2\ g^{-1}$) | $R_m$ | $V_{total}$ ($cm^3\ g^{-1}$) | $V_{micro}$ ($cm^3\ g^{-1}$) | $D_p$ (nm) |
|---|---|---|---|---|---|---|
| $C800NH_3$ | 571.6 | 536.5 | 93.8% | 0.22 | 0.21 | 1.34 |
| $AC800N_2$ | 1371.5 | 1240.2 | 90.4% | 0.53 | 0.49 | 2.64 |
| $AC700NH_3$ | 1309.7 | 1108.7 | 84.6% | 0.50 | 0.44 | 2.90 |
| $AC800NH_3$ | 1510.7 | 1306.1 | 86.5% | 0.74 | 0.62 | 1.97 |
| $AC900NH_3$ | 1428.8 | 998.6 | 72.4% | 0.73 | 0.48 | 2.04 |

**Table 2** Concentrations (*at.* %) of C, O, and N in the different samples and binding energy (B.E., eV) and relative proportions (R.P., %) of the different forms of the doped N obtained by fitting the XPS peaks.

| Sample | C | O | N | pyridinc-N | | pyrrolic-N | | graphitic-N | | pyridine-N-oxide | |
|---|---|---|---|---|---|---|---|---|---|---|---|
| | | | | B.E. | R.P. | B.E. | R.P. | B.E. | R.P. | B.E. | R.P. |
| $AC800N_2$ | 91.32 | 8.38 | 0.30 | 398.2 | 40.61 | 400.0 | 32.41 | 401.5 | 16.28 | 402.8 | 10.64 |
| $AC800NH_3$ | 91.33 | 8.18 | 0.49 | 398.8 | 42.51 | 400.2 | 24.75 | 401.3 | 19.07 | 402.6 | 15.67 |

**Figure Captions:**

**Fig. 1 (**a) Optical image of the luffa sponge. (b-e) SEM images of the $AC800NH_3$ sample at different magnifications.

**Fig. 2** TEM images of the $AC800NH_3$ sample (a) at low and (b) high magnification.

**Fig. 3** XRD patterns (a), Raman spectra (b), $N_2$ adsorption-desorption isotherm (c), and pore distribution (d) of the different samples: I-$C800NH_3$, II-$AC800N_2$, III-$AC700NH_3$, IV-$AC800NH_3$, V-$AC900NH_3$.

**Fig. 4** (a) XPS survey spectra of $AC800N_2$ (I) and $AC800NH_3$ (II). (b) N1s spectrum of $AC800N_2$, (c) N1s spectrum of $AC800NH_3$. (d) FTIR spectra of different samples: I- $C800NH_3$, II-$AC800N_2$, III-$AC700NH_3$, IV-$AC800NH_3$, V-$AC900NH_3$.

**Fig. 5** (a) CV curves of the different samples in 1M $Na_2SO_4$ solution at the scan rate of 20 mV $s^{-1}$: I-$C800NH_3$, II-$AC800N_2$, III-$AC700NH_3$, IV-$AC800NH_3$, V-$AC900NH_3$; (b-d) CV curves of $AC800NH_3$ in the electrolytes of 1 M $Na_2SO_4$ (b), 6 M KOH (c), and 1 M $H_2SO_4$ (d) at different scan rates.

**Fig. 6** (a) Nyquist plots for the different samples in 1 M $Na_2SO_4$ solution: I-$C800NH_3$, II-$AC800N_2$, III-$AC700NH_3$, IV-$AC800NH_3$, IV-$AC900NH_3$, (b) Nyquist plots of $AC800NH_3$ in different electrolytes: (I) 1 M $Na_2SO_4$, (II), 6 M KOH, (III) 1 M $H_2SO_4$.

**Fig. 7** (a) CD curves of the different samples in $Na_2SO_4$ solution at 1A $g^{-1}$: I-$C800NH_3$, II-$AC800N_2$, III-$AC700NH_3$, IV-$AC800NH_3$, IV-$AC900NH_3$: (b-d) CD curves of $AC800NH_3$ at different current densities in 1 M $Na_2SO_4$ (b), 6 M KOH (c), and 1 M $H_2SO_4$ (d) electrolytes.

**Fig. 8** Cycling stability of $AC800NH_3$ in $Na_2SO_4$ (I), KOH (II), and $H_2SO_4$ (III) solutions.

**Fig. 9** CV curves (a) and CD curves (b) of the symmetric supercapacitors assembled with the $AC800NH_3$ materials and an optical image showing a red LED powered by two supercapacitors in series (c).

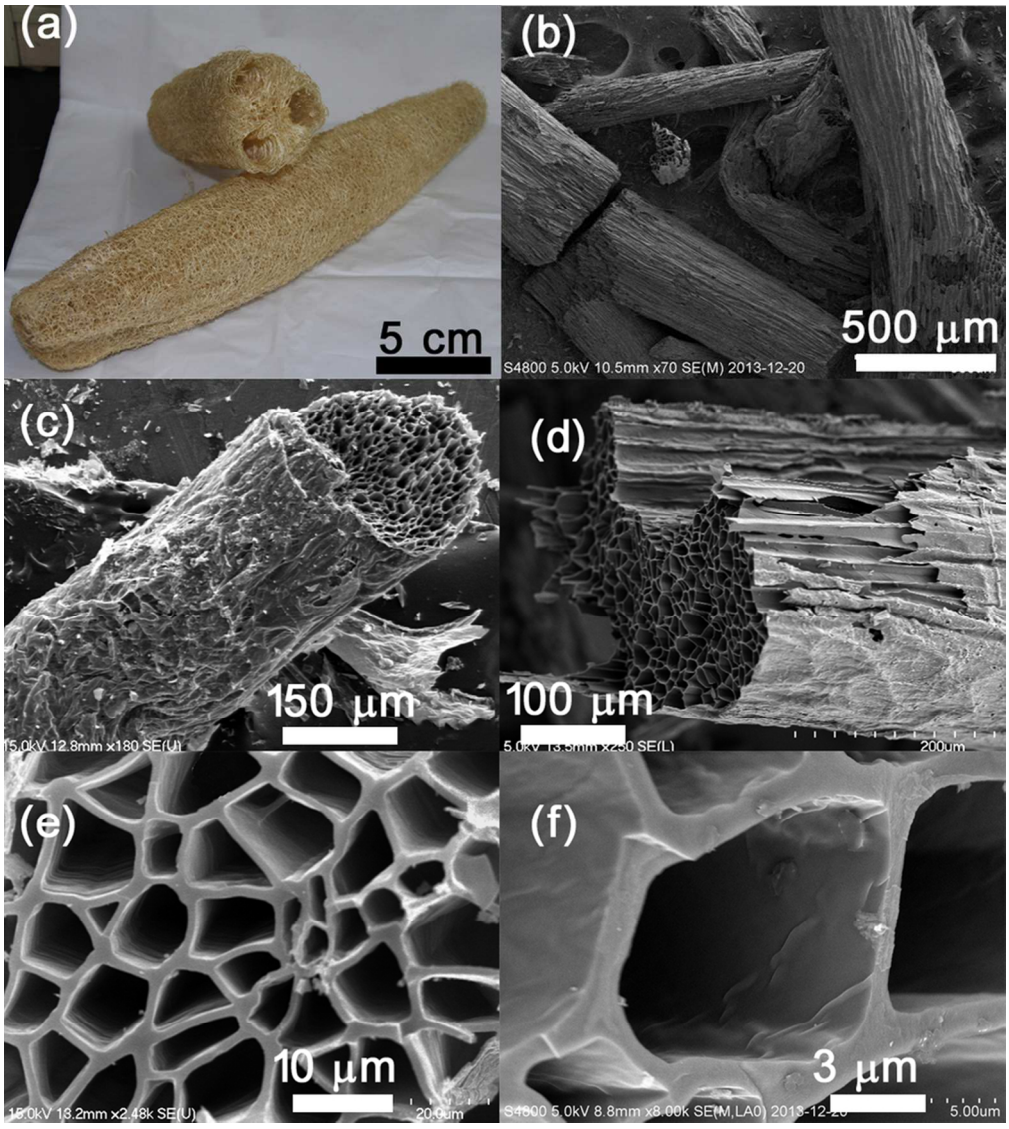


Fig. 1 (a) Optical image of the luffa sponge. (b-e) SEM images of the AC800NH3 sample at different magnifications.
90x101mm (300 x 300 DPI)

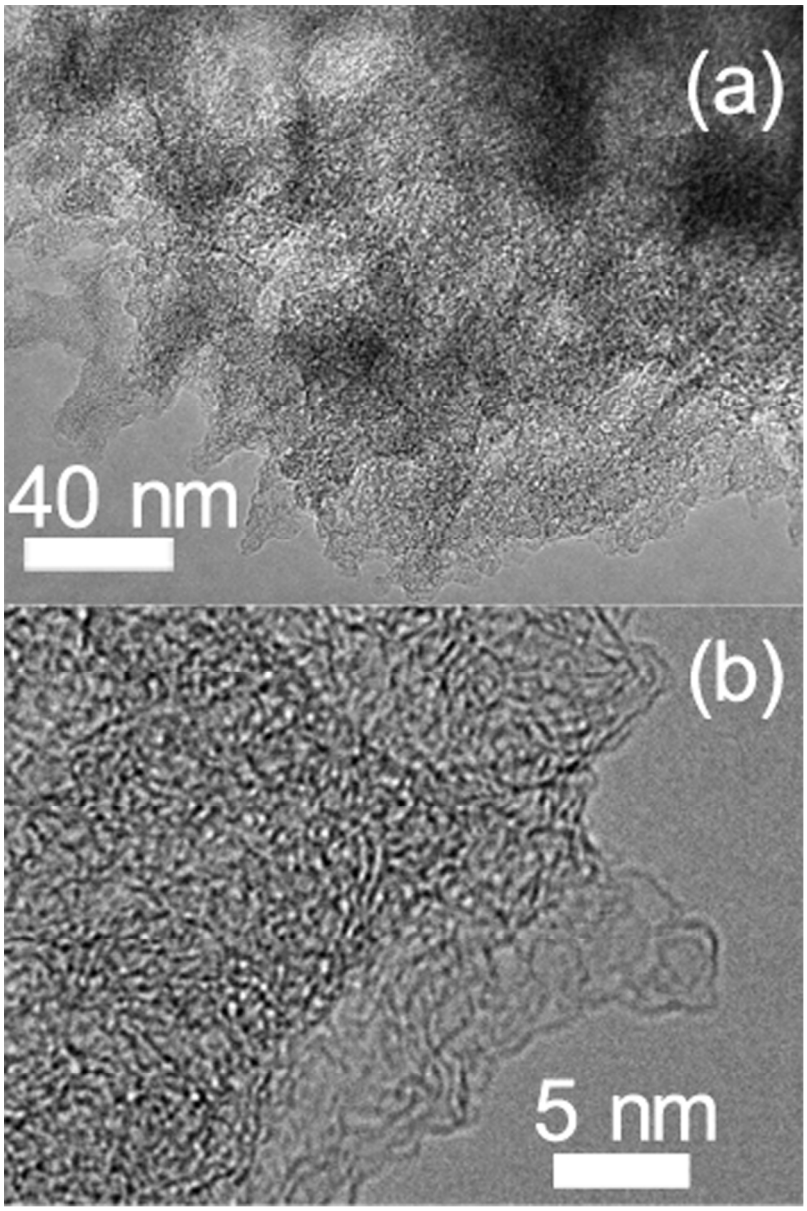


Fig. 2 TEM images of the AC800NH3 sample (a) at low and (b) high magnification.
100x151mm (300 x 300 DPI)

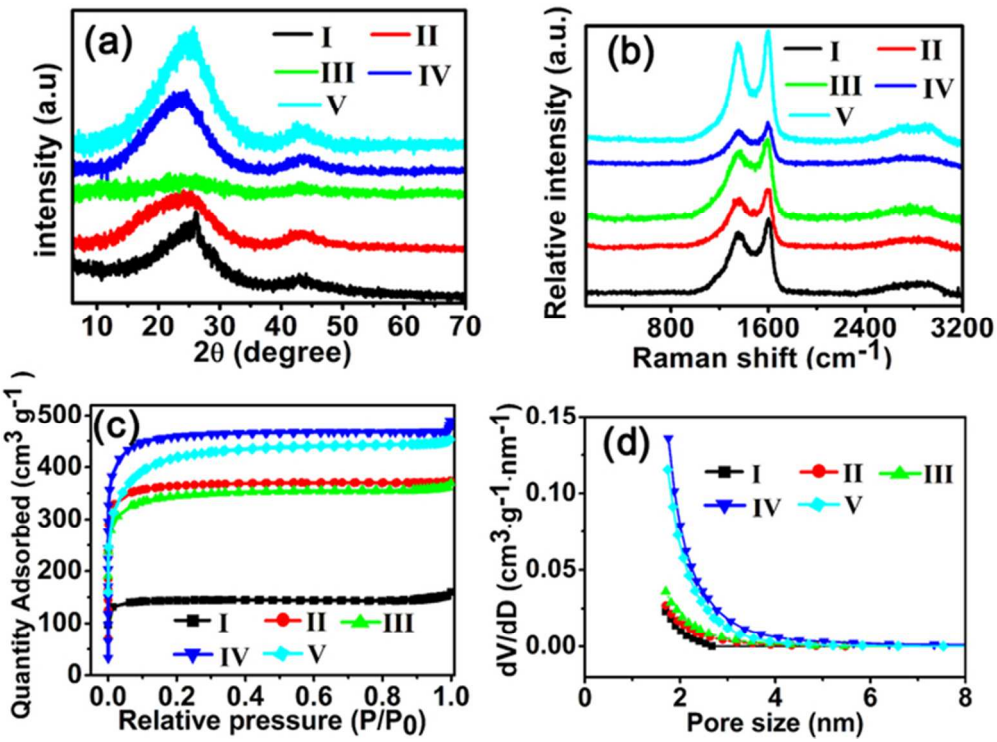


Fig. 3 XRD patterns (a), Raman spectra (b), N2 adsorption-desorption isotherm (c), and pore distribution (d) of the different samples: I-C800NH3, II-AC800N2, III-AC700NH3, IV-AC800NH3, V-AC900NH3.
60x44mm (300 x 300 DPI)

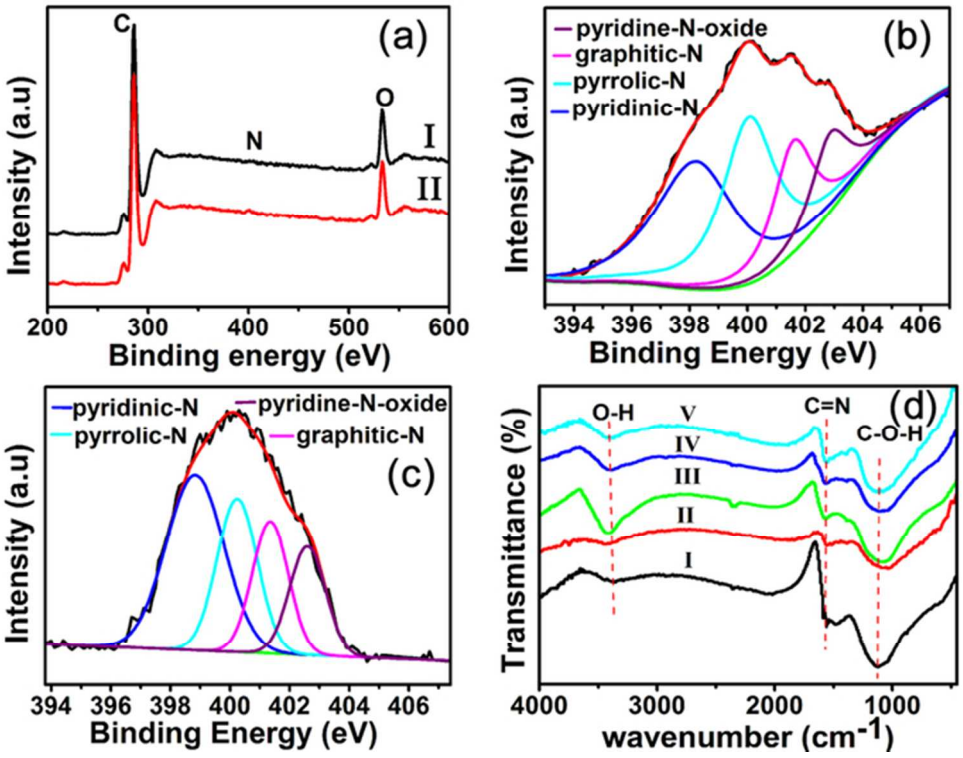


Fig. 4 (a) XPS survey spectra of AC800N2 (I) and AC800NH3 (II). (b) N1s spectrum of AC800N2, (c) N1s spectrum of AC800NH3. (d) FTIR spectra of different samples: I- C800NH3, II-AC800N2, III-AC700NH3, IV-AC800NH3, V-AC900NH3.
60x45mm (300 x 300 DPI)

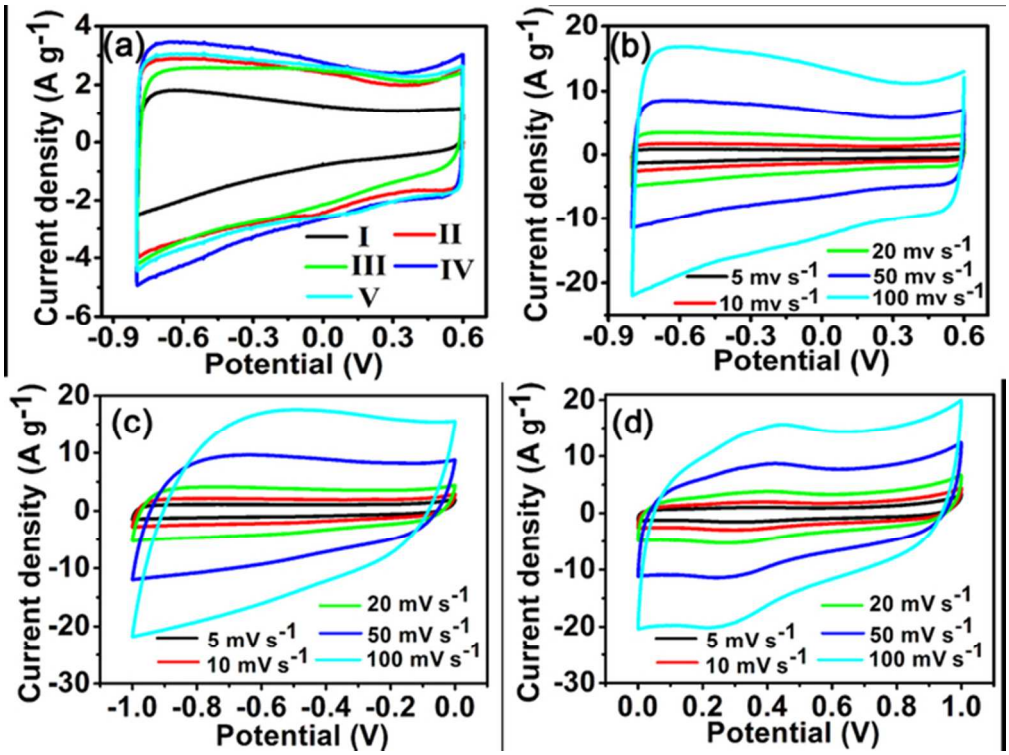


Fig. 5 (a) CV curves of the different samples in 1M Na2SO4 solution at the scan rate of 20 mV s-1: I-C800NH3, II-AC800N2, III-AC700NH3, IV-AC800NH3, V-AC900NH3; (b-d) CV curves of AC800NH3 in the electrolytes of 1 M Na2SO4 (b), 6 M KOH (c), and 1 M H2SO4 (d) at different scan rates.
59x44mm (300 x 300 DPI)

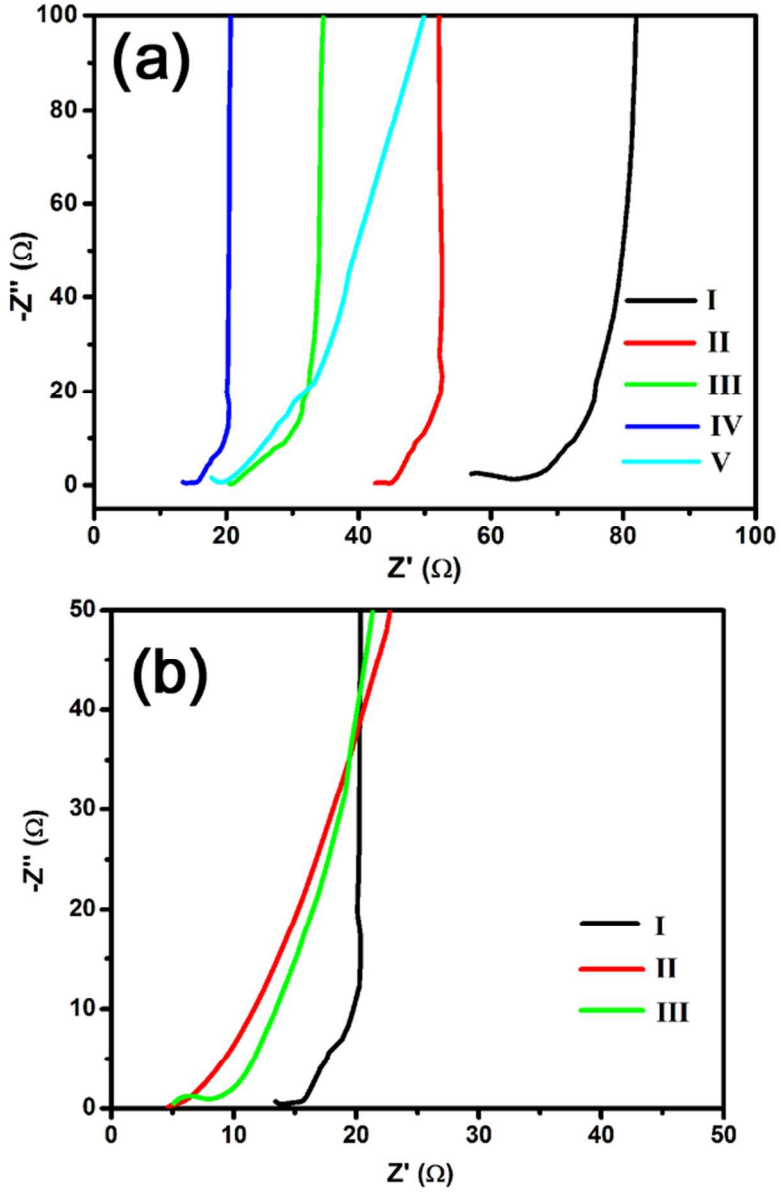


Fig. 6 (a) Nyquist plots for the different samples in 1 M Na2SO4 solution: I-C800NH3, II-AC800N2, III-AC700NH3, IV-AC800NH3, IV-AC900NH3, (b) Nyquist plots of AC800NH3 in different electrolytes: (I) 1 M Na2SO4, (II), 6 M KOH, (III) 1 M H2SO4.
95x143mm (300 x 300 DPI)

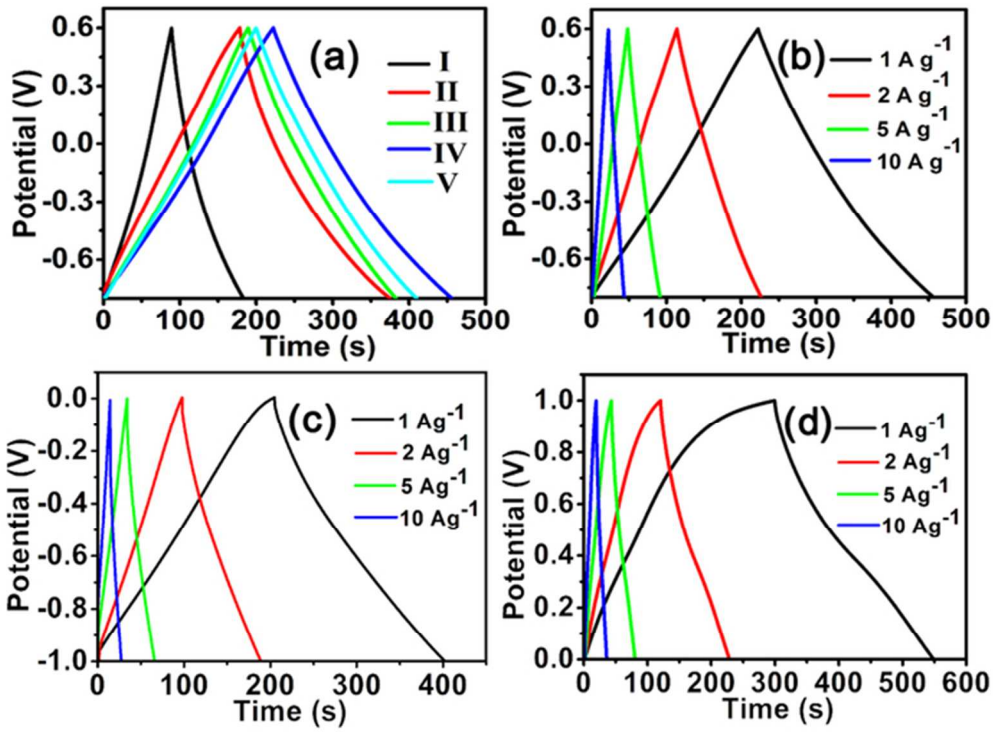


Fig. 7 (a) CD curves of the different samples in Na2SO4 solution at 1A g-1 : I-C800NH3, II-AC800N2, III-AC700NH3, IV-AC800NH3, IV-AC900NH3: (b-d) CD curves of AC800NH3 at different current densities in 1 M Na2SO4 (b), 6 M KOH (c), and 1 M H2SO4 (d) electrolytes.
58x43mm (300 x 300 DPI)

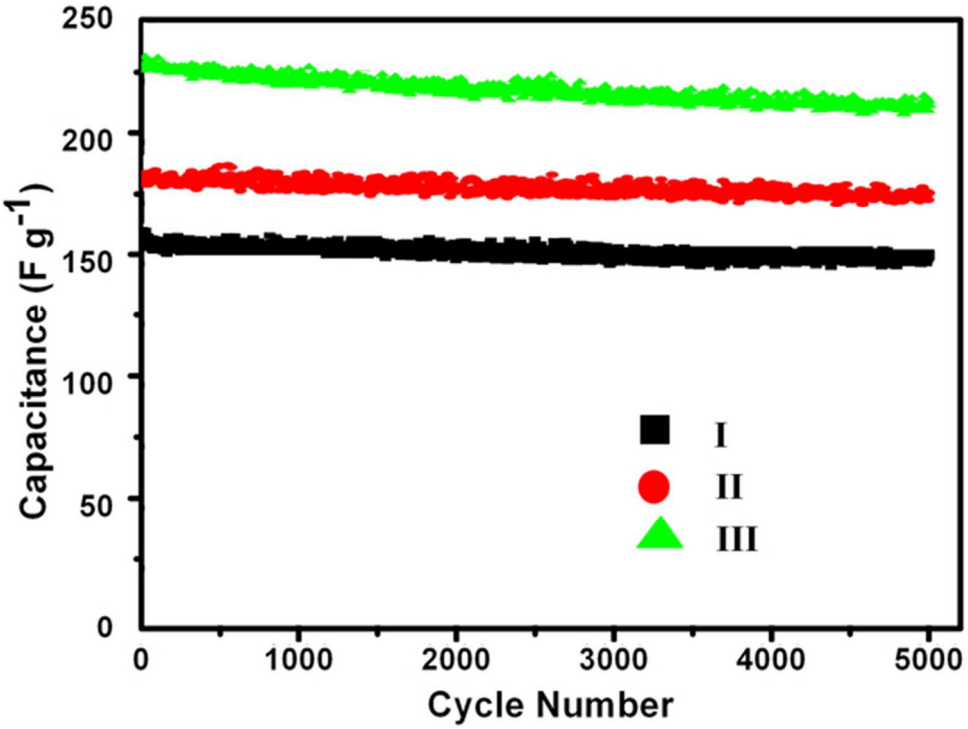


Fig. 8 Cycling stability of AC800NH3 in Na2SO4 (I), KOH (II), and H2SO4 (III) solutions.
54x39mm (300 x 300 DPI)

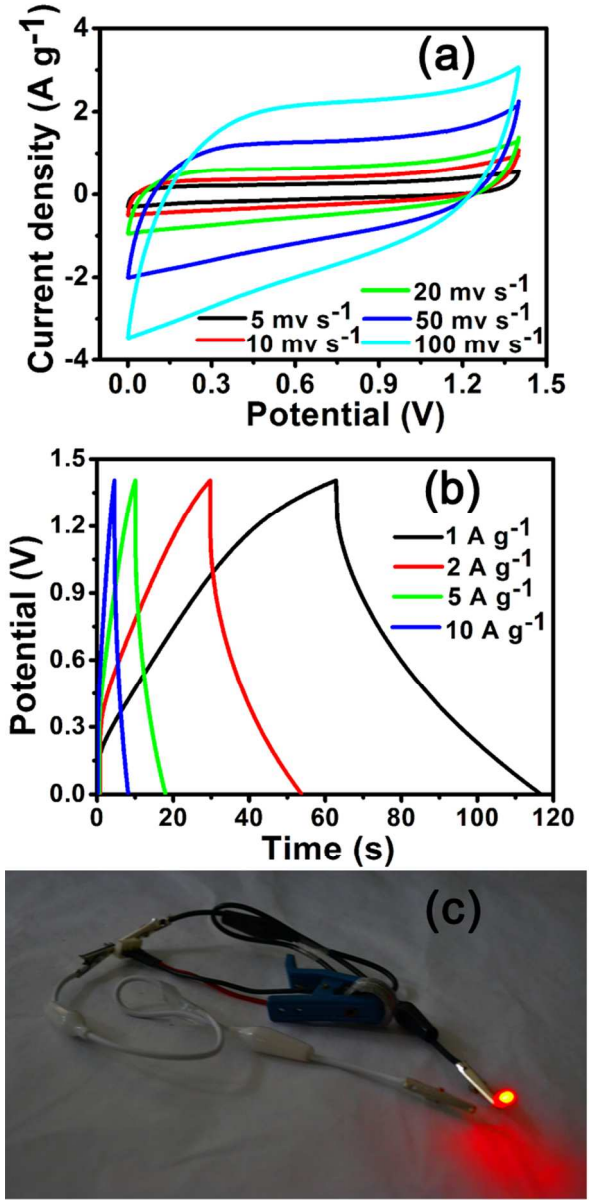


Fig. 9 CV curves (a) and CD curves (b) of the symmetric supercapacitors assembled with the AC800NH3 materials and an optical image showing a red LED powered by two supercapacitors in series (c).
144x297mm (300 x 300 DPI)